Low porosity, high areal-capacity Prussian blue analogue electrodes enhance salt removal and thermodynamic efficiency in symmetric Faradaic deionization with automated fluid control

Erik R. Reale,[a] Lyle Regenwetter,[a] Adreet Agrawal,[a] Brian Dardon,[a] Nicholas Dicola,[a]
Sathvik Sanagala,[a] and Kyle C. Smith[a,b,c,d,*]

a. Department of Mechanical Science and Engineering, University of Illinois at Urbana-Champaign, Urbana IL, USA
b. Department of Materials Science and Engineering, University of Illinois at Urbana-Champaign, Urbana, IL, USA
c. Computational Science and Engineering Program, University of Illinois at Urbana-Champaign, Urbana, IL, USA
d. Beckman Institute for Advanced Science and Technology, University of Illinois at Urbana-Champaign, Urbana, IL, USA

*corresponding author's email: kcsmith@illinois.edu

Abstract

Prussian blue analogues (PBAs) show great potential for low-energy Faradaic deionization (FDI) with reversible Na-ion capacity exceeding 4 mol/L in the solid-state. However, past continuous-flow demonstrations using PBAs in FDI were unable to desalinate brackish water to potable levels using single-pass architectures. Here, we show that recirculation of effluent from a symmetric cation intercalation desalination cell into brine/diluate reservoirs enables salt removal exceeding 80% at thermodynamic efficiency as high as 80% when cycled with 100 mM NaCl influent and when controlled by a low-volume, automated fluid circuit. This exceptional performance is achieved using a novel heated, alkaline wet phase inversion process that modulates colloidal forces to increase carbon black aggregation within electrode slurries to solidify crack-free, high areal-capacity PBA electrodes that are calendered to minimize cell impedance and electrode porosity. The results obtained demonstrate the need for co-design of auxiliary fluid-control systems together with electrode materials to advance FDI beyond brackish salinity.

1.0 Introduction

With more than half of humanity presently facing freshwater scarcity for one month during a given year (Mekonnen and Hoekstra, 2016), desalination of sea and brackish waters could increase freshwater access (Elimelech and Phillip, 2011). However, recent analysis estimates that roughly 1.5 units of concentrated brine are generated globally for every unit of desalinated water, averaged across all water sources, sectors, and technologies (Jones et al., 2019). Depletion of natural freshwater sources motivates the need for new water treatment technologies while also combatting climate change by consuming less energy and replacing aging infrastructure (Mauter and Fiske, 2020). While reverse osmosis (RO) presently comprises the majority of global desalination capacity (Jones et al., 2019), large RO plants are required to achieve high energy efficiency and RO is limited to brine concentrations lower than 1.6 mol/L as monovalent salt, assuming an 80 bar limit for spiral wound RO pressure vessels (Subramani and Jacangelo, 2014). Electrically driven desalination processes avoid the mechanical limitations of RO by separating dissolved ions rather than H_2O molecules. Among such processes (Suss et al., 2015; Tang et al., 2019), Faradaic deionization (FDI) using cation intercalation materials (CIMs) shows great promise on the basis of reversible Na concentrations in the solid-state (namely 5.0 mol/L for the Prussian blue analogue investigated here with 65 mAh/g charge capacity and 2 g/cc nominal density) exceeding seawater salinity (0.5 mol/L as NaCl) by ten-fold. Techno-economic analysis of FDI and comparison with the more frequently studied capacitive deionization (CDI) shows the former method outputs more desalinated water at lower cost while being a more compact technology, in part due to CIMs having greater capacity (Metzger et al., 2020). Despite our early modeling that introduced a symmetric Na-ion battery architecture to desalinate seawater using CIMs (Liu and Smith, 2018; Smith, 2017; Smith and Dmello, 2016), subsequent experimental demonstrations thereof failed to realize more than 30% salt removal from continuously flowing brackish water (Kim et al., 2017; Porada et al., 2017; Reale et al., 2019). We posit here that efficiency losses within auxiliary systems must be understood in conjunction with electrode-scale transport processes to extend FDI using CIMs beyond brackish salinity.

The configuration of electrolyte flow through porous electrodes (Liu and Smith, 2018; Reale et al., 2019; Smith, 2017; Son et al., 2020) and charge transport within porous electrodes (Reale et al., 2019; Shrivastava and Smith, 2018) are known to affect rate capability and energy consumption in FDI using symmetric CIM electrodes, but past results suggest that unknown mechanisms remain and prevent the salt-removal potential of CIMs from being accessed. In FDI, saltwater can flow through a gap between electrodes in a flow-by configuration or directly through the porous structure of electrodes sandwiched within a cell in a flow-through configuration. Flow-through electrodes incorporating Prussian blue analogue (PBA) CIMs, which we first demonstrated (Reale et al., 2019), have shown improved salt removal (Smith, 2017), charge utilization (Liu and Smith, 2018; Smith, 2017; Son et al., 2020), and specific energy consumption (Smith, 2017; Son et al., 2020) compared to flow-by PBA electrodes due to charge-efficiency loss at electrode/channel interfaces in flow-by (Liu and Smith, 2018; Smith, 2017) and smaller ohmic drop in flow-through (Son et al., 2020). Further, our experiments introducing flow-through FDI achieved rapid salt removal with one order of magnitude lower specific energy consumption, as provided by judicious choice of electronically conductive additives (Reale et al., 2019) and inspired by our earlier work demonstrating that nanoparticle agglomeration limits transport in electrodes containing PBAs (Shrivastava and Smith, 2018). However, charge efficiency diminished at higher current densities due to low utilization shortening cycle time, an effect that complementary modeling indicated was likely a result of strong salt concentration gradients in both the streamwise and transverse directions within porous electrodes (Reale et al., 2019).

Along those lines, our past modeling revealed that streamwise salt concentration gradients in feedwater result in streamwise state-of-charge gradients in CIMs within the porous electrodes through which feedwater flows (Liu and Smith, 2018). While such state-of-charge gradients lead to efficiency loss and decreased CIM capacity utilization, we predicted that recirculation of feedwater can minimize such deleterious effects (Liu and Smith, 2018). While recirculation eliminates the coupling between flow rate and salt removal which constrains single-pass architectures, past studies (Liu et al., 2021; Pothanamkandathil et al., 2020; Singh et al., 2020) provided limited detail concerning the approaches used to repeatedly cycle feedwater through a single two-electrode FDI cell, and such studies only demonstrated a cumulative salt removal as high as 40 mM (Singh et al., 2020). Along similar lines, others have flowed feedwater in series through flow compartments in an electrodialysis (ED) stack, while only reducing the salinity of 25 mM influent by 30% (Kim et al., 2017). The development of novel high-capacity electrode materials for electrochemical desalination including CDI and ED has been regarded as unable to significantly reduce energy consumption compared to RO (Patel et al., 2020). However, we show here that improvements can be achieved in FDI through reduction of concentration gradients, increasing electrode conductivity, and development of auxiliary flow-control systems optimizing salt removal in conjunction. Accordingly, we demonstrate and detail for the first time an automated multi-pass FDI architecture using recirculation from brine and diluate reservoirs enabled by custom, low-volume valves and a low-cost Arduino control system.

Beyond such effects, we postulate that the porosity of flow-through FDI electrodes can be engineered to increase degree-of-desalination in flow-through FDI cells. Mass balance on a representative volume element of a porous electrode with porosity ε and CIM volumetric loading ν suggests that decreasing porosity from as-cast values of 85% (Reale et al., 2019) to 67% could increase degree-of-desalination by over three-fold,[†] which is conceivable by calendering electrodes. Calendering, the process of compressing electrodes between two rollers, is known to increase electronic conductivity and improve rate capability (van Bommel and Divigalpitiya, 2012), but decreased porosity and increased tortuosity are known to reduce ionic conductivity (Ebner et al., 2014; Landesfeind et al., 2016; Malifarge et al., 2017). While these competing effects may result in a certain degree of calendering that maximizes FDI performance, the fabrication of thick electrodes with the areal capacity levels needed to create low-porosity electrodes using calendering is a challenge in itself. The reduction of cost and inactive mass in Li-

---

[†] Neglecting volume within electrodes comprised by conductive additives and binder and assuming perfect transmission of solution through porous electrodes, the maximum cation concentration change within solution $(\Delta c)_{soln}$ that could be effected by transferring such cations into a CIM with a reversible cation concentration $(\Delta c)_{solid}$ is given by $(\Delta c)_{soln}/(\Delta c)_{solid} = (1-\varepsilon)/\varepsilon$.

ion batteries (Gallagher et al., 2016) has motivated development of alternative electrode fabrication processes to yield high areal capacity (Zolin et al., 2019) due to the tendency of conventionally-prepared electrodes to crack during drying after slurry casting. To this end, we use a wet-phase inversion (WPI) process that eliminates the capillary-bridge induced cracking that arises during solidification by drying. While we (Bhat et al., 2019; Reale et al., 2019; Reale and Smith, 2018) and others (Lim et al., 2009) have used WPI to fabricate electrodes for FDI and capacitive deionization using a room temperature pure water bath, here we introduce a heated, alkaline WPI process inspired by the Derjaguin-Landau-Verwey-Overbeek (DLVO) theory of inter-particle forces in colloids (Goodwin, 2009). The DLVO theory has previously predicted percolation thresholds in simulated dispersions (Maria et al., 2015) and is applied here towards slurry constituents to induce solidification of thick, high-conductivity electrodes that we subsequently calender. While past simulations based on Brownian dynamics of conductive particles in electrode slurries predicted that larger particles form conductive paths more easily (Cerbelaud et al., 2015), our previous experiments (Reale et al., 2019) on slurries containing PBA nanoparticles and carbon black showed trends opposite those simulations. Rather than expecting particles to pack together randomly as in Brownian dynamics, we posit per DLVO theory that van der Waals and electrostatic forces influence their dynamics to a degree dependent on particle radii, zeta potential, and Hamaker constants of the associated particles and on the dielectric properties of intervening fluid. While the interplay between such forces has been simulated for Li-ion battery electrodes, showing variations in electrode microstructure dependent on the mass fraction, particle size, and temperature of both CIM and additive particles (Zhu et al., 2014, 2011), few studies (Cho et al., 2007) have previously exploited understanding of such interactions in experimental electrode fabrication. In doing so, our colloid-inspired electrode fabrication process results in more electronically conductive and mechanically stable electrodes that do not crack at high cast thicknesses. Calendering of these electrodes increases their density and electronic conductivity, which is shown to enhance salt removal and thermodynamic efficiency in FDI.

A brief outline of this article follows. We first discuss a novel wet phase inversion process and the effects of electrode calendering, which we use in conjunction to fabricate electrodes with low porosity, high areal capacity, and high rate capability. We then present results for the cycling of such electrodes in FDI desalination experiments. In such experiments we employ a custom lab-scale recirculating FDI cell to alternate flow paths such that feedwater in one reservoir continuously desalinates while another reservoir simultaneously concentrates. After several cycles using the densest electrodes, the diluate reservoir reached 90% salt removal from 100 mM NaCl influent before reaching a limit caused by desalinated and concentrated effluent mixing reducing charge efficiency. The use of denser electrodes is further shown to decrease energy consumption, achieving 80% thermodynamic energy efficiency (TEE) at 80% salt removal.

2. Materials and Methods

2.1 Electrode fabrication, conductivity measurements, and flooded cell characterization:

PBA nanoparticles and associated slurries were prepared as in our previous work (Reale et al., 2019; Shrivastava and Smith, 2018) with electrodes composed of 85 wt% nickel hexacyanoferrate (NiHCF) PBA, 5 wt% EC-600JD Ketjen black, and 10 wt% Solef polyvinylidene fluoride (PVDF) binder. The first electrodes were cast at 150 μm thick onto 100 μm thick 2010A high-purity graphite foil current collector (Ceramaterials), and subsequent electrodes were cast at higher thicknesses of 250 μm and 320 μm as described in the Results and Discussion Section. After being cast and solidified using wet phase inversion (WPI, as described subsequently), the electrodes were calendered using an MTI roll press to a targeted thickness of 150 μm, as measured by an MTI thickness gauge. Porosity was then calculated from the densities of the total electrode and its solid constituents, $\varepsilon = 1 - \rho_{electrode}/\rho_{solid}$. Electrochemical cycling of these electrodes was performed at several C-rates in a 1M NaCl flooded cell versus a Ag/AgCl reference electrode with a graphite counter electrode.

We used WPI to solidify electrodes after casting. Here, an as-cast slurry film supported on a current collector is immersed in a water bath to displace n-methyl-2-pyrrolidone (NMP) solvent and solidify the PVDF binder dissolved therein to form a mechanically stable electrode (Bhat et al., 2019; Reale et al., 2019; Reale and Smith, 2018). While previous WPI processes used room temperature deionized water baths for phase inversion, we explored modified bath conditions to improve electrode properties. Initial tests were done using 1 μm Al_2O_3 particles (AdValue Technology) as a surrogate for PBA material due to supply limitations for the latter material, as in our previous work optimizing electrode conductivity without calendering (Reale et al., 2019). As Timcal Super C45 carbon black (MTI) had previously been shown to be an inferior conductive additive compared to Ketjen black, C45 was used in initial studies with the expectation that improvements in conductivity would be more obvious than with Ketjen black. To measure the electronic conductivity of electrodes, slurries were cast onto an insulative

PTFE substrate, and conductivity was measured using an in-house built four-point probe (Reale et al., 2019).

To influence the inter-particle forces in slurries, a 200 mL WPI water bath was used to explore the effects of three different experimental parameters: (1) using a hot plate to heat the water between 25°C and 85°C, (2) increasing bath pH from 7 to 12 by adding NaOH, and (3) increasing salt concentration by dissolving NaCl up to 450 mM (see SI Section S3). PBA electrodes immersed in the high pH bath also displayed structural stability when cast at high thickness, solidifying at 320 μm when an electrode that thick would normally crack during drying if phase inverted using a room temperature, neutral pH water bath.

2.2 FDI system design and control:

The custom built FDI cell used in our previous study (Reale et al., 2019) was employed for desalination experiments in conjunction with a custom recirculating fluid circuit built around it (see Fig. 4, SI Section S1, and Video S1). The FDI cell used two PBA electrodes separated by a Neosepta AMX anion exchange membrane (Astom Corp). In all desalination experiments two test tubes were filled with 5 mL of saltwater to be converted to brine and diluate during cycling, with initial concentrations of 100 mM, or 200 mM in a separate experiment. To direct flow, an Arduino controller actuated four servos to pinch branching paths of rubber tubing, ensuring that feedwater from only one reservoir flowed through either side of the FDI cell (Video S1). Flow rates of both effluent streams were kept constant and equal by using a Masterflex peristaltic pump, and all experiments used a flow rate of 1 mL/min. This flow rate is 4x higher than our previous experiments with a single-pass system (Reale et al., 2019) to take advantage of the recirculation, keeping concentration gradients low. With the diluate and brine flow rates being equal, the water recovery rate in all experiments was 50%. Images of the complete cell design, details of its fluid circuit, and its electrical control system are found in SI Section S1. Salt concentration at the two inlets and two outlets was measured using four custom-built flow-through conductivity sensors connected to an eDAQ isoPod which recorded conductivity using the program PodVu.

2.3 Desalination experiments

All desalination experiments used a current density of 1 mA/cm^2 applied to 2.5 cm^2 electrodes by a Biologic VMP-3 potentiostat over a voltage window of +/- 0.45V. Based on our measured values of hydraulic permeability, we estimate a pressure drop across the FDI cell of 71.6 kPa and 430 kPa, respectively, for cycling with the least and highest areal-capacity electrodes tested here at a 1 mL/min flow rate. The time delay between OC starting and IV actuation was set to 20 seconds in all FDI experiments, roughly twice the duration of the time delay between IV and OV actuation, to uniformize concentration on the respective sides of the cell. During the OC period before IV actuation, electrochemical impedance spectroscopy (EIS) tests were performed with frequencies ranging from 100 kHz to 100 mHz to study how impedance changes from cycle to cycle. Lower frequencies were not tested because doing so would prolong experiments. The time delay between actuation of IVs and OVs was different for each electrode pair and was calculated using a calibration process described in SI Section S2. Prior to each experiment, the conductivity probes used were calibrated with 100 and 200 mM influent, known to respectively have conductivities of 1.067 and 2.034 S/m at 298K (Chambers et al., 1956).

3.0 Results and Discussion

3.1 Electrode fabrication techniques

We first report on experiments aimed at fabricating high conductivity, high areal-capacity PBA electrodes, predicated on the hypothesis that their use in FDI will increase salt removal. To fabricate PBA electrodes with high areal loading and low porosity we initially used our past WPI procedure (Reale et al., 2019) (using a room temperature deionized (DI) water bath for phase inversion) to fabricate 250 µm thick electrodes that were subsequently calendered to lower thicknesses, yielding electrodes of varied porosity. Figure 1A shows the results for cycling of an electrode with different degrees of calendering using a 1M NaCl flooded cell with a graphite counter electrode and a Ag/AgCl reference electrode. These results indicate that as electrode thickness and porosity decrease, electrode rate capability Increases. Between rates of 2.6C and 10.3C, utilization of an uncalendered 250 µm electrode reduced by 64%, while the same electrode calendered down to 72 µm showed only an 18% reduction in utilization and 34% greater capacity at 2.6C relative to 250 µm electrodes at the same rate. Returning to the lowest C-rate after cycling each sample at 10.3C confirmed that the capacity drops observed at high rate were not due to electrode degradation. Despite the concern of low porosity increasing ionic resistance in porous electrodes (Ebner et al., 2014; Landesfeind et al., 2016), calendered electrodes showed no rate capability decrease due to lost pore volume. However, we found that electrodes cast at thickness greater than 250 µm readily cracked when using conventional WPI, motivating our search for improved electrode fabrication conditions.

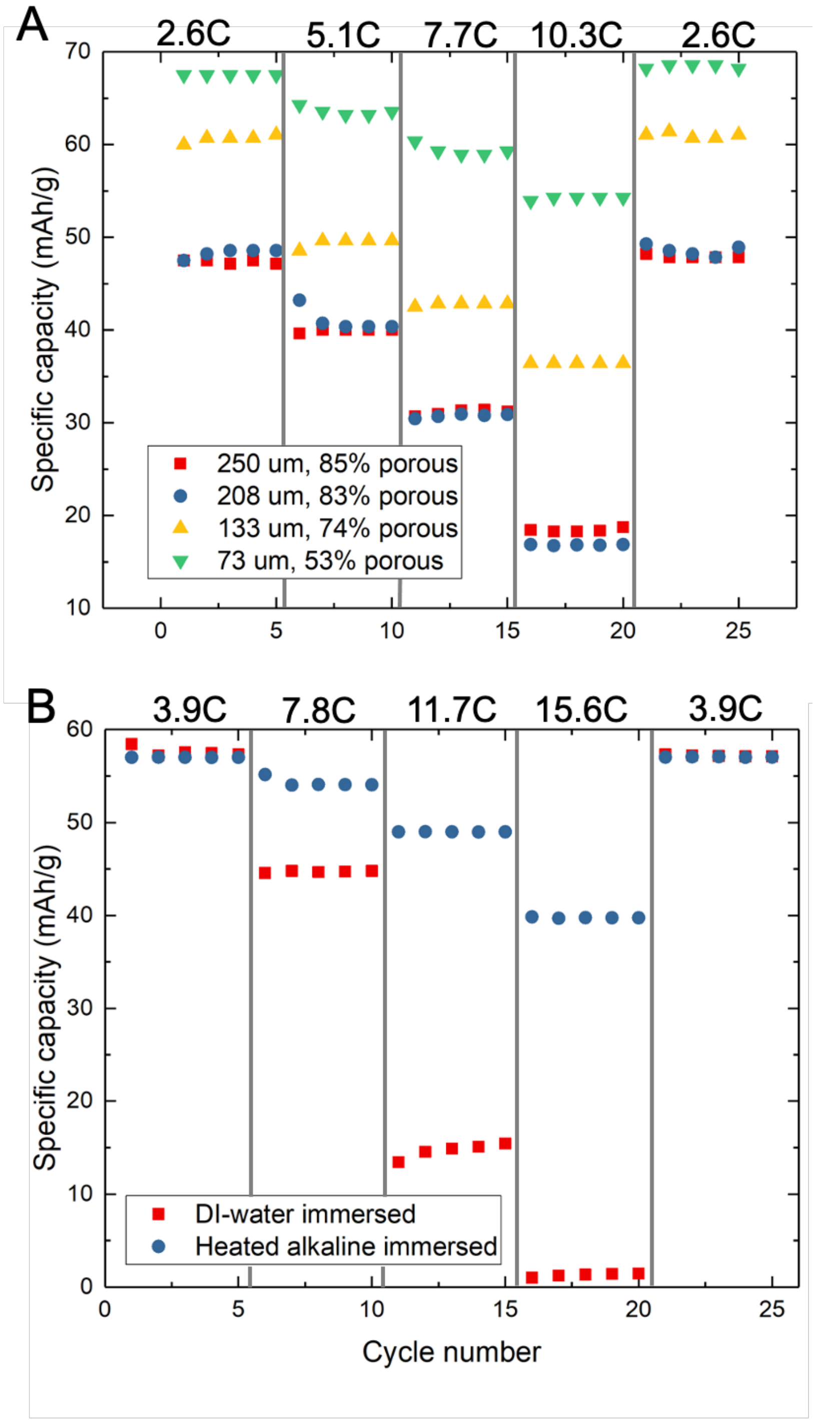

Figure 1: (A) Specific capacity for a PBA electrode fabricated with conventional WPI at different degrees of calendering at different C-rates. (B) Capacities of uncalendered

electrodes fabricated with conventional WPI and 85°C, pH 12 water immersed electrodes. All cycling experiments were performed in a 1M NaCl flooded cell.

To overcome areal loading limitations and increase electrode performance overall, we analyzed the colloidal interactions between particles in electrode slurry occurring during WPI processes. We postulate that the forces between active (PBA) and conductive (carbon black) particles during microstructure formation of an electrode can be engineered to promote aggregation of conductive particles and increase effective electronic conductivity. To guide our investigation of such we employ DLVO theory, the application of which suggests that decreased conductor-active particle aggregation is achievable by conductors and active particles having like-signed zeta potential, making them mutually repulsive (see SI Section S3). Furthermore, DLVO theory suggests that temperature affects electrostatic interactions. Subsequently, we alter WPI bath conditions and show that repulsion between carbon and active particles can be increased, causing more carbon to aggregate into a conductive backbone and yielding increased electronic conductivity.

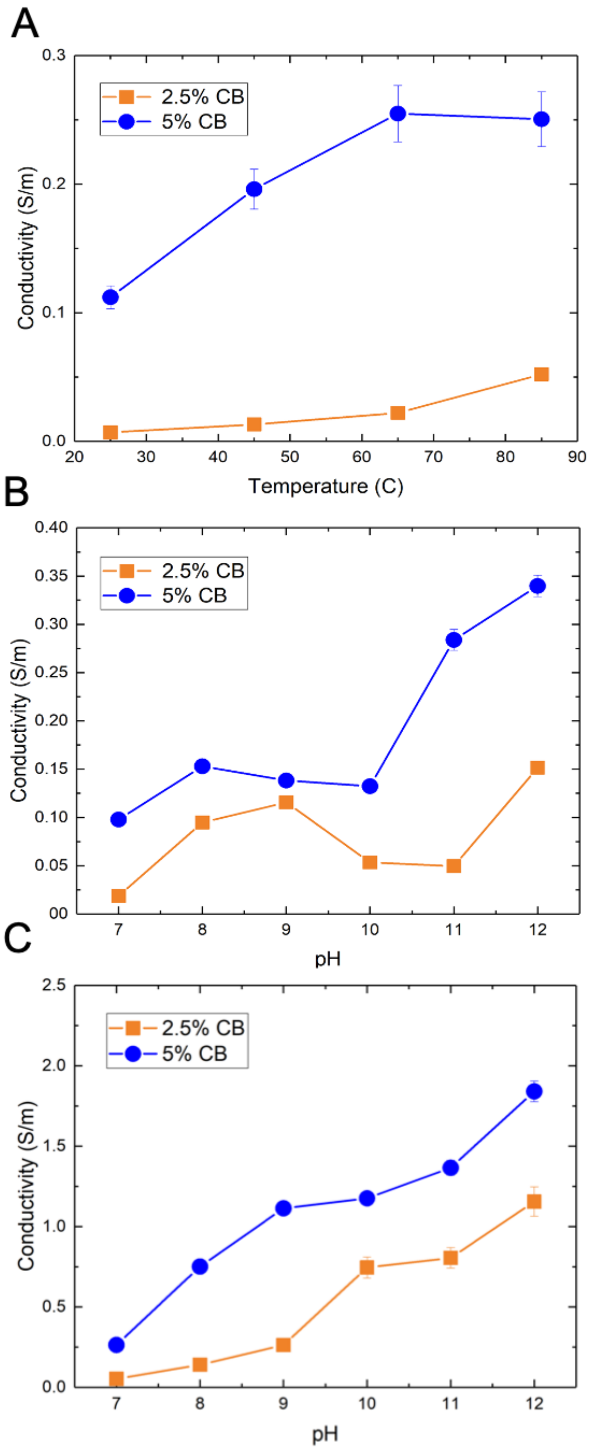

Figure 2: Electronic conductivity for electrodes with 2.5 and 5 wt% C45 carbon black and surrogate active particles (Al_2O_3) made using (A) increasing bath temperature and (B) increasing bath pH. Error bars are found from the 5 μm variability in electrode thickness which determines how conductivity is calculated using a four-point probe. (C) Electronic conductivity for electrodes made at 85°C using an alkaline bath.

Accordingly, we performed modified WPI experiments on cast electrode slurries to characterize the effects of the temperature and pH of inversion baths on electronic conductivity, so as to modulate electrostatic colloidal interactions respectively via Debye length and zeta potential. To do this we formulated slurries comprised of conductive particles (C45 carbon black) and surrogate particles replacing low-conductivity PBA (Al_2O_3). Figures 2A and 2B show variations of electronic conductivity respectively with temperature and pH, where temperatures of 80-90ºC and pH 12 are shown to produce 2-3 times higher conductivity than the baseline case at room temperature and neutral pH when 5 wt.% carbon black is used. The changes in electronic conductivity observed among the different WPI conditions, despite containing the same constituent mass fractions, are qualitatively consistent with DLVO theory. Increasing pH causes zeta potential to decline for both particle phases, and a sufficient increase thereof can cause surrogate active particles to become negatively charged (Singh et al., 2005). However, carbon black particles have been found to possess negative zeta potential at pH 7 (Sis and Birinci, 2017), indicating that surrogate active particles and carbon black experience strong electrostatic attraction at pH 7. Because increasing pH beyond 7 causes carbon black particles to have increasingly negative zeta potential, carbon and surrogate active particles repel each other in alkaline solution. Additionally, increasing bath temperature gives carbon particles more kinetic energy to overcome potential energy barriers, increasing the likelihood of carbon particle aggregation. Variations of the corresponding potential energy curves are presented in the SI to illustrate these concepts (Section S3).

Because the third condition for the WPI bath, dissolution of inert salt, produced mild effects on electrode formulation (see SI Section S3), we next explored the potential for synergistic interactions of increased temperature and pH to enhance electrode formulation. Figure 2C shows that the resulting electronic conductivity, obtained for a bath heated at 85ºC using different levels of alkaline pH, increases to a greater degree than when using modified temperature or pH conditions separately. In electrodes containing 2.5 wt% carbon black, conductivity increased by up to 167 times compared to electrodes immersed in room-temperature DI water.

Informed by findings obtained with surrogative active material and C45 carbon black, we subsequently used WPI bath conditions that yielded highest electronic conductivity (85ºC and pH 12) to fabricate PBA electrodes containing Ketjen black conductor, for which our previous work (Reale et al., 2019) demonstrated improved electronic conductivity relative to C45 carbon black. Flooded cell cycling comparing WPI processes was performed, shown in Fig. 1B. The electrode wet-phase inversed in a heated, alkaline bath showed superior rate capability compared to electrodes prepared using standard conditions, which is consistent with the results obtained with surrogate material that showed increased electronic conductivity under such conditions. In addition, the modified WPI conditions were shown to prevent cracking of electrodes with thicknesses as large as 320 μm, despite an electrode immersed in 85°C, neutral pH water cracking at 320 μm. This finding confirms the critical role of WPI bath pH in preserving the thick electrodes' mechanical integrity. We postulate that binder-solution interactions, such as the Hofmeister effect (Thormann, 2012), may also increase binder uniformity within electrodes and consequently increase mechanical strength.

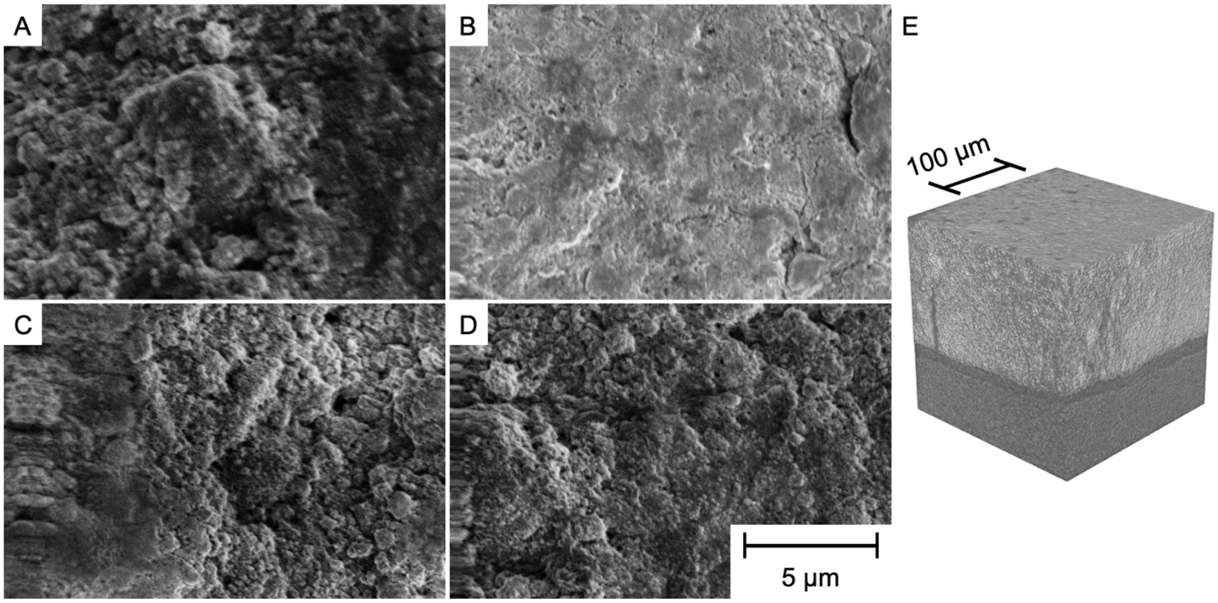

Figure 3: SEM Images of a conventional PBA electrode (A) before calendering and (B) after calendering. Images (C) and (D) show a heated, alkaline-bathed electrode before and after calendering, respectively. All four images use the same scale bar. (E) X-ray CT image of a calendered PBA electrode (light gray) prepared using the modified WPI process supported on graphite foil (dark gray).

To acquire visual evidence for the effect of electrode fabrication conditions on their microstructure, SEM images of DI water-immersed and heated alkaline-immersed electrodes were obtained (Fig. 3), including images taken before and after calendering to 50% of their initial thickness. While the microstructures of uncalendered electrodes prepared using conventional and modified WPI processes were indistinguishable (Figs. 3A, 3C), WPI conditions were shown to affect the texture of calendered electrodes substantially (Fig. 3B and 3D). Specifically, the conventional WPI process produced a relatively smooth and occluded calendered surface compared with the modified WPI process, consistent with the postulate that increased pH and temperature during WPI increases binder uniformity throughout electrodes. This observation is also consistent with the results of flooded-cell cycling which showed improved rate capability for electrodes prepared using the modified WPI process. Fig. 3E shows an X-ray computed tomography (CT) scan of a calendered electrode prepared by modified WPI, confirming the process yields a homogeneous distribution of PBA particles within the microstructure over a 200 μm by 200 μm area. However, a larger area of 620 μm by 790 μm reveals defective fissures constituting approximately 5% to 10% of the overall volume in the electrode (Fig. S11 and Video S2). To understand the impact of such fissures, we measured these electrodes' hydraulic permeability using a simple gravity-driven apparatus (Reale et al., 2019). The densest calendered electrodes had a permeability of 0.23 μm^2 compared with the uncalendered electrodes' 1.38 μm^2 due to their decreased porosity and average micropore radius. This finding indicates that flow is forced through the microporous regions of these electrodes and is therefore not "short-circuited" through defective fissures. These results for electrode microstructure, flooded cell cycling, and electronic conductivity motivated use of the modified WPI process and electrode calendering with CIMs in a cation intercalation desalination FDI cell.

3.2 Recirculating FDI desalination performance

FDI experiments were conducted using an in-house custom-built flow cell and integrated fluid recirculation system (Figs. 4A-4D), detailed in SI Section S1. Valves at the outlets (OVs) and inlets (IVs) of both electrodes direct salt water respectively to and from the reservoirs for brine (BR) or diluate (DR), as shown in Figs. 4B and 4C. Figure 4E shows the corresponding variations of cell voltage and influent salt concentrations with time, the latter measured by conductivity probes at the inlet regions of both electrodes when the cell is subjected to galvanostatic cycling with either positive (PC) or negative (NC) current, followed by a brief open-circuit (OC) period. In addition to constructing the cell with the lowest internal volume possible by using narrow inner diameter tubing and custom parts dimensioned to minimize volume, experiments were conducted to optimize valve timing to reduce mixing between diluate and brine streams. Pause periods were added at the end of each PC/NC period, minimizing mixing by accounting for residence time in the internal volume of the system, as described in Section S2 of the SI. Hence, Figure 4E and Video S1 show a finite-time delay between switching events of electrical current and both IVs and OVs, denoted as 'IVs switch' and 'OVs switch.' After calibrating such events we observed salt concentration varying linearly with time during initial cycles and that salt removal per cycle declined during successive cycles due to diluate and brine effluent streams mixing.

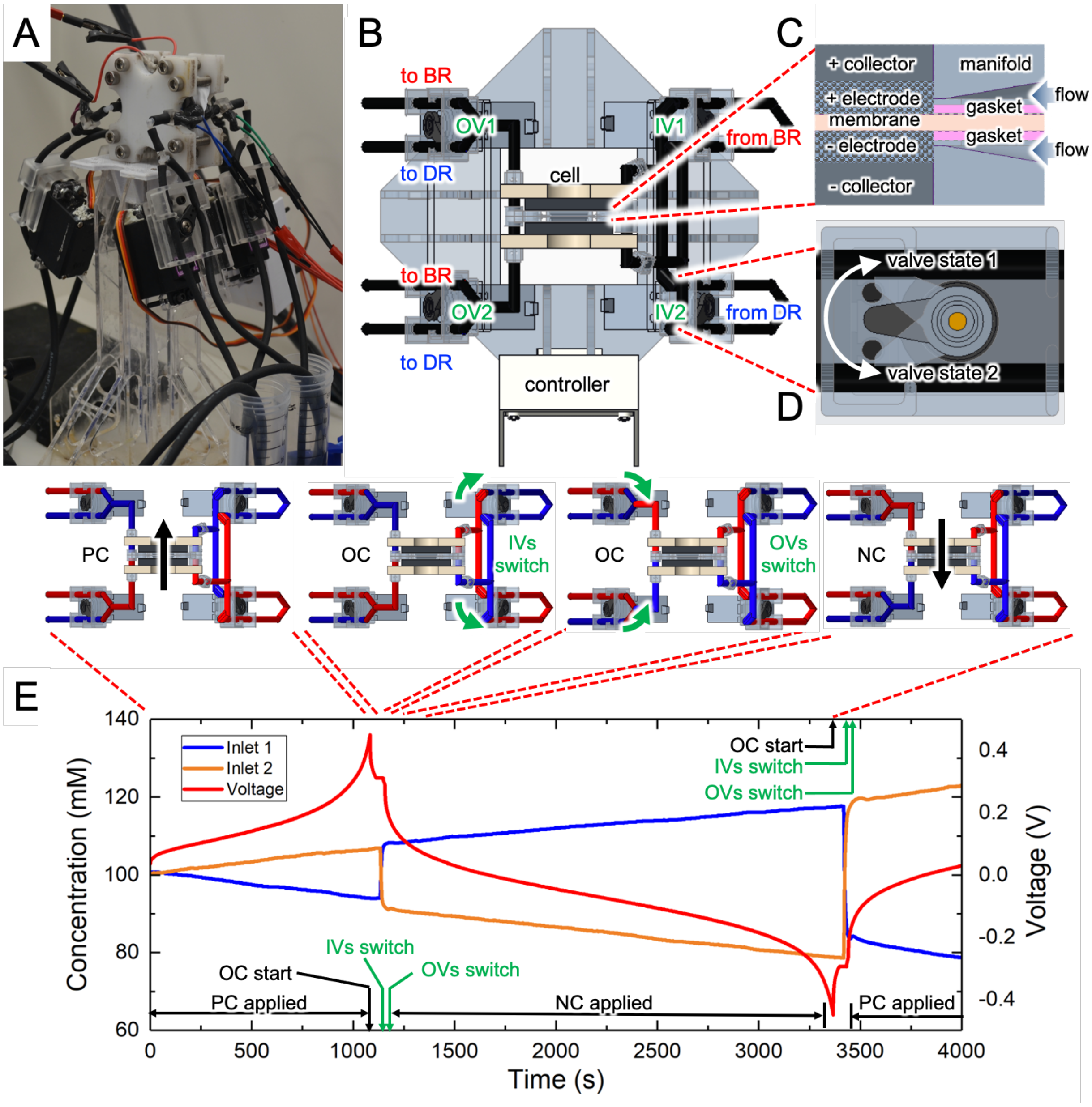

Figure 4: (A) Photograph of the recirculating FDI system incorporating inlet valves (IVs) and outlet valves (OVs) that direct fluid to/from electrodes from/to a brine reservoir (BR) and a diluate reservoir (DR). (B) Top view of the cell showing valve locations. Detailed views of (C) the inlet region of the cell showing PBA symmetric electrodes sandwiching an anion exchange membrane (AEM) and (D) of valve switching actions. The time sequence of cell voltage and salt concentration used to conduct one complete cycle is shown using inset diagrams together with the timing of valve and current switching events controlled automatically. PC, OC, and NC respectively denote positive current, open circuit, and negative current.

Using this apparatus with the electrical/fluidic cycling sequences already described, we explored the effect of PBA electrode formulation on FDI performance. As a point of reference, use of this recirculating FDI apparatus with electrodes having the same formulation, porosity (85%), and areal loading (5.3 mg-PBA/cm^2) as in our previous work (Reale et al., 2019) yielded 65% salt removal from 100 mM NaCl solution, in contrast with <27% salt removal in our previous single-pass experiments. We then tested electrodes cast at 250 μm thick, solidified with WPI using room-temperature DI water, and calendered to 150 μm thick, yielding 8.7 mg-PBA/cm^2 and 75% porosity. The corresponding experiments produced 80% salt removal, owing to the increased capacity and reduced mixing volume between brine and diluate effluent from denser electrodes. The third pair of electrodes was first cast and solidified by WPI in 85°C water with pH 12, resulting in a 320 μm electrode that was subsequently calendered down to 150 μm, yielding 11.1 mg-PBA/cm^2 and 67% porosity. This further increase of areal loading and decrease of porosity produced a maximum salt removal of 90% from 100 mM influent, corresponding to a productivity of 3.3 L/hour-m^2. A final test using 200 mM influent with the 11.1 mg-PBA/cm^2 electrodes was performed. Because the electrodes removed more salt per half-cycle, 104 mM was removed from the 200 mM influent before becoming limited by mixing, due to increased ionic conductivity and decreased concentration polarization improving capacity utilization.

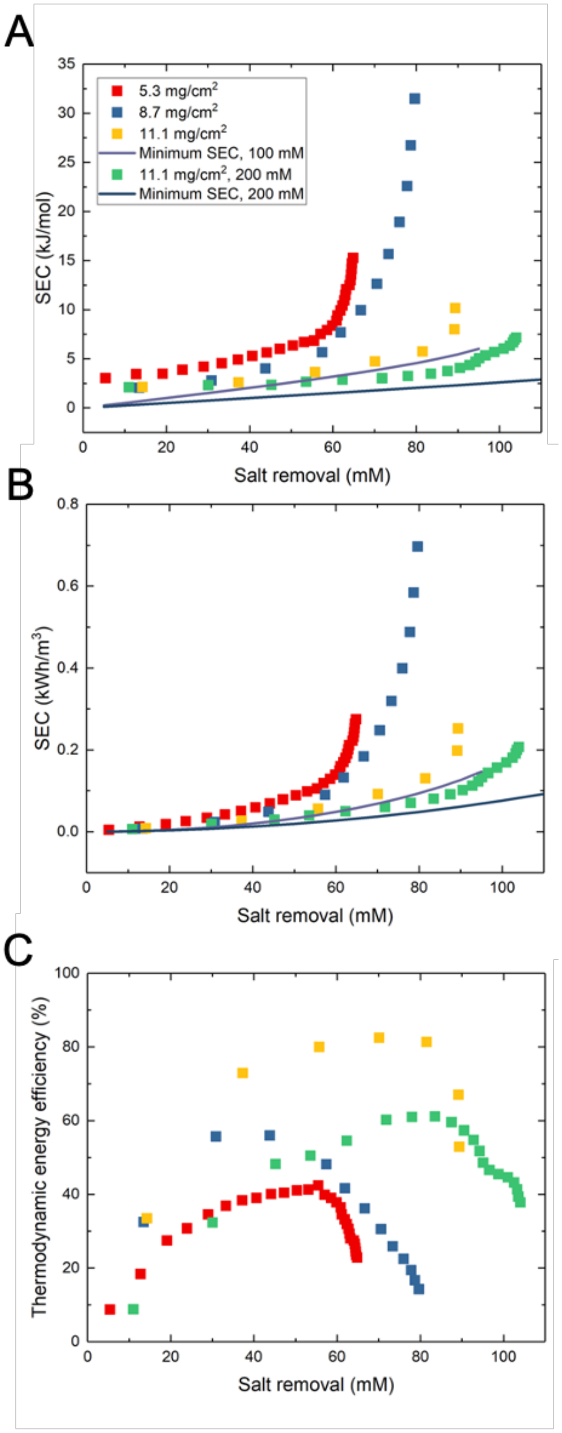

Figure 5: SEC versus salt removed from the diluate reservoir in units of (A) kJ/mol and (B) kWh/m^3. We note that the thicker electrodes are, the greater the concentration change after each cycle due to the extended desalination time and fewer mixing opportunities during switching. (C) Thermodynamic energy efficiency for the three electrode pairs.

These high salt removals, achieved using different electrode densities, yielded different levels of specific energy consumption (SEC) to reduce influent concentration c_i to diluate concentration c_d, as shown in Fig. 5A and calculated by the equation $SEC = E_{total}/(c_{i-}c_d)\forall_{resevoir}$. Units of kWh/m^3 are an alternate method of expressing SEC shown in Fig. 5B, omitting concentration and calculated as $SEC = E_{total}/\forall_{resevoir}$. We note that these SEC values are calculated based on the cumulative energy invested and the cumulative salt removal achieved, rather the energy invested and salt removed per cycle. Due to the high electronic conductivity and active particle loading of electrodes produced by the modified WPI process, the FDI system achieved excellent salt removal at an SEC that approaches the thermodynamic minimum separation energy, $SEC_{minimum} = 2RT\left(c_d ln(c_d) + \left(\frac{1}{\gamma} - 1\right) c_b ln(c_b) - \frac{c_i}{\gamma} ln(c_i)\right)/(c_i - c_d)$ where γ is the water recovery rate of 0.5 and c_b is brine concentration. As we show later, decreased energy consumption with increased electrode density is supported by its low ohmic resistance (see Fig. 7A and discussion thereof). Our previous work using the same cell operating at the same current density (1 mA/cm^2) in single-pass mode showed a simulated SEC of 2.7 kJ/mol (Reale et al., 2019), while the 5.3 mg/cm^2 electrodes sharing the same composition have an initial SEC of 3.04 kJ/mol. As the present system reached the limit of salt removal due to the mixing of diluate and brine, further cycling consumed significantly more energy, causing SEC to rise steeply while salt removal stagnated. Because all experiments used the same flow rate and current density, the average salt absorption rate (ASAR) was initially 0.55-0.6 μmol/cm^2-min for all three experiments. ASAR declines with the mixing effect decreasing removal each cycle, becoming 0.51 μmol/cm^2-min on average when the experiment with 11.1 mg/cm^2 electrodes concluded.

At the highest salt removal with 100 mM influent, the thermodynamic energy efficiency (TEE) of the recirculating cell, defined as $TEE = SEC_{minimum}/SEC$, was 50%, but TEE reached as high as 80% for the densest electrodes before mixing outweighed the electrodes' ability to remove salt in a single cycle (Fig. 5C). One reason for the high TEE is the high salt removal shown in Fig. 5A, where SEC for all three electrodes increases linearly with salt removal during early cycles. At low salt removal, the thermodynamic minimum is low compared to the experimental SECs, but as both experimental and theoretical SECs increase, the ratio between them increases as well. The present 100 mM influent is more ionically conductive than the 20-50 mM influents used in other studies, and the denser, highly conductive electrodes created here consume less energy due to smaller ohmic losses that we show subsequently. It should also be noted that the cell operated at only 1 mA/cm^2, and SEC for similar electrodes increased approximately linearly with current density in our past work (Reale et al., 2019).

While such results demonstrate the practical benefits of high areal loading for increased desalination performance, inspection of specific capacity attained from cycle to cycle revealed trends suggesting further room for improvement. Fig. 6A shows that utilization of charge capacity declined with increasing salt removal, though high areal capacity electrodes retain the most capacity. When comparing the 8.7 mg/cm^2 and 11.1 mg/cm^2 electrodes, the former electrodes only utilize 45% of their capacity at 80% salt removal, while at the same salt removal the latter electrodes retained 87% utilization. This outcome is likely a result of high areal-capacity electrodes producing greater *flow efficiency*, defined as the ratio between time for the electrodes' porous volume to be replaced and the charging time (Hawks et al., 2018). Because denser electrodes have smaller pore volume, feedwater is removed fast enough to supply fresh sodium ions for intercalation into PBA particles, and between the lowest and highest areal loadings, flow efficiency increases by 30%. The specific capacity of electrodes during experiments with 200 mM remained high even when the cell reached the limits of its salt removal due to abundant sodium in solution. Though the flow rate was four times higher than what our single-pass experiments previously used (Reale et al., 2019) (0.25 mL/min), decreasing charge capacity at high salt removal suggests that gradients of salt concentration and PBA state-of-charge decrease utilization. However, the disparate concentrations of salt in diluate and brine streams near the end of FDI processes are also expected to produce concentration polarization and ohmic polarization limiting capacity when performing galvanostatic cycling within a finite cell voltage window. The inability of the system to continue removing salt also causes charge efficiency to decline (Fig. 6B), eventually reaching zero. During a single half-cycle, charge efficiency remains at 80-95% as salt is continuously removed, but cumulative charge efficiency approaches zero due to mixing counteracting salt removal.

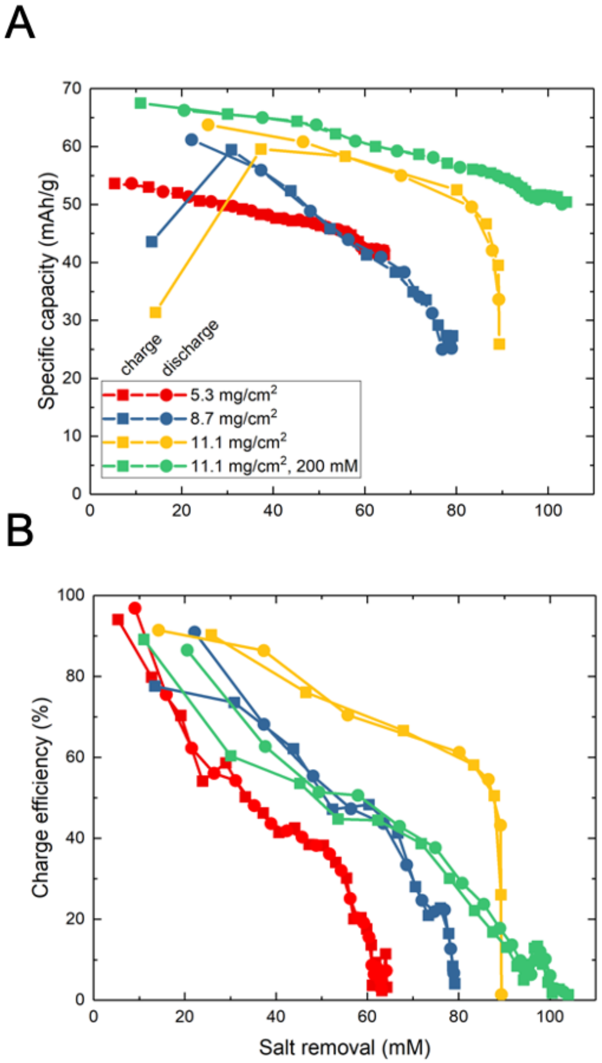

Figure 6: (A) Specific capacity during charging and discharging versus the salt removed from the diluate stream. Initial data points for charging appear low because the electrodes were already partially charged before the experiment began. (B) Charge efficiency versus salt removed from the diluate stream for the same experiments.

To analyze the influence of cell impedance on desalination performance we conducted electrochemical impedance spectroscopy (EIS) during the open circuit (OC) periods of each cycle (Fig. 7A). These spectra show that real impedance at high frequency gradually increases from cycle-to-cycle, as a result of one side of the cell becoming less ionically conductive during salt removal. This effect is evidenced by the voltage versus capacity curves measured during PC and NC cycling (Fig. 7B), where increased polarization pushes average cell voltage nearer to the edges of the voltage window within which cycling occurs. From the initial cycle to the final cycle, the degree of polarization increase differs with each type of electrode and the final salt removal attained. However, polarization is largest during cycles with highest salt removal, and when real impedance at high frequency is largest.

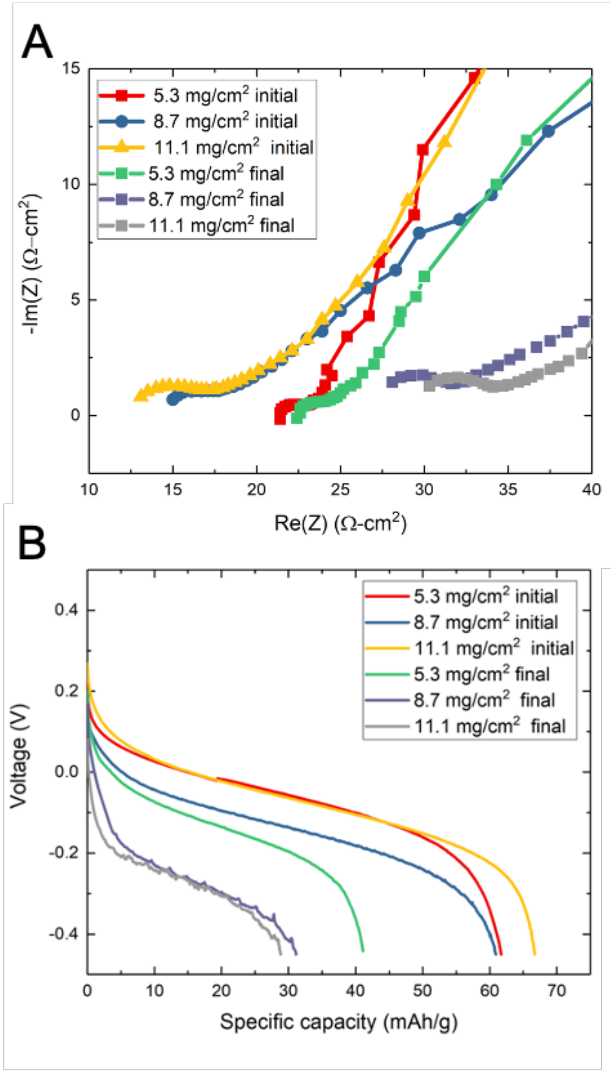

Figure 7: (A) EIS curves for the three pairs of electrodes following the initial and final half-cycles of each experiment. We note that the more densely calendered electrodes show lower real impedance at high frequencies. (B) Voltage versus specific capacity curves for the initial discharging and the final charging half-cycles of the three electrode pairs, showing diminishing utilization and increasing polarization at high salt removal. For ease

of viewing the polarization differences, the final charging curves were made to have a negative sign.

In Fig. 7A electrodes with 5.3 mg/cm^2 show little change in real impedance between the first and final cycles, despite attaining 65% salt removal. However, real impedance at high-frequency in the denser electrodes increased more than two-fold. This limited change of impedance for electrodes with lower areal capacity can be understood by assuming that ionic conductivity is directly proportional to salt concentration. Equation 1 shows the theoretical ratio between ionic resistance at a certain concentration difference $R_{ion}(\Delta c)$ and the initial resistance when both anode and cathode contain influent of the same concentration, neglecting the intervening AEM.

$$\frac{R_{ion}(\Delta c)}{R_{ion}(t=0)} = \frac{1}{2}\left(\frac{1}{1-\frac{\Delta c}{c_0}} + \frac{1}{1+\frac{\Delta c}{c_0}}\right) \tag{1}$$

This simple relation reveals that only at 71 mM of salt removal from 100 mM does the theoretical ionic resistance double. Furthermore, ionic resistance within electrodes is only one source of impedance, including electronic resistance, Warburg impedance, AEM impedance, and contact resistance in external circuitry. The minor influence of concentration is further demonstrated in Section S2 of the SI. In any case, Fig. 7B shows the increasing impedance with increasing salt removal in cell voltage curves. Average voltage during the first and final half-cycles increased from 0.07V to 0.29V as the 11.1 mg-PBA/cm^2 achieved 90% salt removal, lowering utilization and limiting maximum salt removal. Calendering electrodes increased electronic conductivity and reduced ohmic energy losses, keeping energy consumption low at high salt removal.

Finally, Table 1 compares energy consumption achieved recently in FDI using symmetric electrode architectures. As each work tested an FDI system at different current densities and flow rates, the values shown are for the highest salt removal achieved. The present results show slightly higher ASAR than most cases and achieved an excellent 90% salt removal, a higher fraction than any other listed. The final SEC of 10.9 kJ/mol is also high due to the mixing effect. However, at 80% salt removal an SEC of 5.7 kJ/mol was achieved, approaching the thermodynamic minimum energy of 4.5 kJ/mol for that salt removal level and reaching a record level of thermodynamic energy efficiency of 80%.

Table 1: Comparison of performance among symmetric FDI systems, including SEC, ASAR, and the percent salt removed from the initial concentration of each study. MHCF compounds denote different Prussian blue analogue materials using a certain inactive transition metal M in its lattice, while AEM and CEM denote anion and cation exchange membranes, respectively. Values in parentheses indicate those obtained at optimal thermodynamic energy efficiency (TEE), whereas the remaining values are shown for those obtained at maximum salt removal.

SEC (kJ/mol)	ASAR (μmol/cm^2-min)	Influent salinity (mM)	Diluate salinity (mM)	% Salt Removal	Active material and separator	Other comments	Ref. no.
10.9 (5.7)	0.51	100	10 (20)	90 (80)	NiHCF/AEM /NiHCF	parallel flow-through; recirculating	this work
7.16	0.46	200	96	52	NiHCF/AEM /NiHCF	parallel flow-through; recirculating	this work
18.0	2.73	100	73	27	NiHCF/AEM /NiHCF	parallel flow-through	(Reale et al., 2019)
10.1	0.45	20	17.5	12.5	carbon/CEM /carbon	transverse flow-through; carbon cloth modified with silane groups	(Arulrajan et al., 2019)

6.44	0.31	477	286.2	40	NiHCF/AEM /FeHCF	no flow	(Lee et al., 2017)
2.4	0.34	25	17.5	30	CuHCF/AEM/ CuHCF	flow-by	(Kim et al., 2017)
5.6	0.25	500	400	20	NiHCF/CEM/ AEM /CEM/FeHCF	Nafion-coated particles, flow-by divided by membranes	(Ahn et al., 2020a)
27.0	6.2	500	100	80	Ag/CEM /AgCl	no flow	(Ahn et al., 2020b)
13.76	0.534	50	35	30	CuHCF/AEM/ CuHCF	parallel flow-through	(Son et al., 2020)
21.1	3.85	50	41.7	16.7	BiOCl/CEM /BiO	parallel flow-through	(Liu et al., 2021)
23.04	0.104	20	15	25	NiHCF/AEM /NiHCF	recirculating	(Pothanamkandathil et al., 2020)

4.0 Conclusions

In this work a recirculating flow-through Faradaic deionization apparatus was demonstrated and shown to produce 90% salt removed from one reservoir of 100 mM aqueous NaCl, transferring the salt into a second reservoir of brine with 50% water recovery rate. In the same experiment, 80% salt removal was achieved with a TEE of 80%. It was shown that recirculating cell performance is limited by diluate and brine mixing during valve-switching processes, the effects of which were minimized through the use of an open-circuit period during which the inlet and outlet valves were switched at different times. Such pause periods improved performance relative to preliminary tests, however they could not totally eliminate mixing effects, resulting in an upper limit for salt removal and a lower limit for specific energy consumption that is highest for porous cation intercalation electrodes with high areal capacity and low porosity. We showed this by fabricating electrodes using a novel wet phase inversion process incorporating a heated, alkaline water bath for the first time to solidify electrodes with high areal capacity that were subsequently calendered to achieve simultaneously low porosity. Impedance spectra measured during the open-circuit periods of FDI cycling showed that the electronic resistance of electrodes was reduced by their calendering, and flooded cell experiments showed better utilization.

Despite the significant improvements demonstrated relative to prior work, limitations other than electrode areal capacity make further increases in salt removal unattainable for the current cell even with the present recirculating apparatus. For example, reducing the ratio of internal fluid volume to the pore volume of electrodes is likely to lead to further improvements in desalination performance, further decreasing the effect of mixing between brine and diluate streams. However, the degree of apparent mixing is likely to include the effects of diffusion and dispersion at interfaces between diluate and brine streams. Pumping power remains significant, approximately 0.12 kWh/m^3 for the densest electrodes during each pass of water. Over the complete desalination process, this energy consumption is multiplied by over 50x due to the same fluid being recirculated, making pumping energy exceed the electrical energy by an order of magnitude. Thus, pumping power should be targeted as another area for improving FDI performance. These results motivate other approaches to minimize losses that arise due to such effects, including scale-up of the FDI cell. The current FDI cell possesses pore volume, when incorporating the lowest porosity electrodes tested (67%), that is 70% of the total volume within tubing and manifold supplying influent to the electrodes. An FDI cell with increased capacity – constructed using more electrode area with similar areal capacity – would increase total electrode pore volume in proportion to cell capacity, while holding tube volume constant.

Acknowledgments

The US National Science Foundation (Award no. 1931659) and the Department of Mechanical Science and Engineering at the University of Illinois at Urbana-Champaign (UIUC) supported this research. Scanning electron microscopy (SEM) was performed at the Materials Research Laboratory at UIUC, and X-ray computed tomography (CT) was performed at the Beckman Institute for Advanced Science and Technology. We thank Fitz Chem LLC for providing Ketjen black material.

References

Ahn, J., Kim, S., Jeon, S. il, Lee, C., Lee, J., Yoon, J., 2020a. Nafion-coated Prussian blue electrodes to enhance the stability and efficiency of battery desalination system. Desalination 114778. https://doi.org/10.1016/j.desal.2020.114778

Ahn, J., Lee, Jiho, Kim, S., Kim, C., Lee, Jaehan, Biesheuvel, P.M., Yoon, J., 2020b. High performance electrochemical saline water desalination using silver and silver-chloride electrodes. Desalination 476, 114216. https://doi.org/10.1016/j.desal.2019.114216

Arulrajan, A.C., Ramasamy, D.L., Sillanpää, M., Wal, A. Van Der, Biesheuvel, P.M., Porada, S., Dykstra, J.E., 2019. Exceptional Water Desalination Performance with Anion-Selective Electrodes 1–5. https://doi.org/10.1002/adma.201806937

Bhat, A.P., Reale, E.R., Smith, K.C., Cusick, R.D., 2019. Reducing impedance to ionic flux in capacitive deionization with Bi-tortuous activated carbon electrodes coated with asymmetrically charged polyelectrolytes. Water Res. X 3, 100027. https://doi.org/10.1016/j.wroa.2019.100027

Cerbelaud, M., Lestriez, B., Videcoq, A., Ferrando, R., Guyomard, D., 2015. Understanding the Structure of Electrodes in Li-Ion Batteries: A Numerical Study. J. Electrochem. Soc. 162, A1485–A1492. https://doi.org/10.1149/2.0431508jes

Chambers, J.F., Stokes, J.M., Stokes, R.H., 1956. Conductance of Concentrated Aqueous Sodium and Potassium Chloride Solutions at 25 60, 985–986. https://doi.org/10.1021/j150541a040

Cho, Y.K., Wartena, R., Tobias, S.M., Chiang, Y.M., 2007. Self-assembling colloidal-scale devices: Selecting and using short-range surface forces between conductive solids. Adv. Funct. Mater. 17, 379–389. https://doi.org/10.1002/adfm.200600846

Ebner, M., Chung, D.W., García, R.E., Wood, V., 2014. Tortuosity anisotropy in lithium-ion battery electrodes. Adv. Energy Mater. 4, 1–6. https://doi.org/10.1002/aenm.201301278

Elimelech, M., Phillip, W.A., 2011. The future of seawater desalination: energy, technology, and the environment. Science (80-.). 333, 712–717. https://doi.org/10.1126/science.1200488

Gallagher, K.G., Trask, S.E., Bauer, C., Woehrle, T., Lux, S.F., Tschech, M., Lamp, P., Polzin, B.J., Ha, S., Long, B., Wu, Q., Lu, W., Dees, D.W., Jansen, A.N., 2016. Optimizing Areal Capacities through Understanding the Limitations of Lithium-Ion Electrodes. J. Electrochem. Soc. 163, A138–A149. https://doi.org/10.1149/2.0321602jes

Goodwin, J., 2009. Colloids and Interfaces with Surfactants and Polymers, First. ed. Wiley.

Hawks, S.A., Knipe, J.M., Campbell, P.G., Loeb, C.K., Hubert, M.A., Santiago, J.G., Stadermann, M., 2018. Quantifying the flow efficiency in constant-current capacitive deionization. Water Res. 129, 327–336. https://doi.org/10.1016/j.watres.2017.11.025

Jones, E., Qadir, M., van Vliet, M.T.H., Smakhtin, V., Kang, S. mu, 2019. The state of desalination and brine production: A global outlook. Sci. Total Environ. 657, 1343–1356. https://doi.org/10.1016/j.scitotenv.2018.12.076

Kim, T., Gorski, C.A., Logan, B.E., 2017. Low Energy Desalination Using Battery Electrode Deionization. Environ. Sci. Technol. Lett. 4, 444–449.

https://doi.org/10.1021/acs.estlett.7b00392

Landesfeind, J., Hattendorff, J., Ehrl, A., Wall, W.A., Gasteiger, H.A., 2016. Tortuosity Determination of Battery Electrodes and Separators by Impedance Spectroscopy. J. Electrochem. Soc. 163, A1373–A1387. https://doi.org/10.1149/2.1141607jes

Lee, J., Kim, S., Yoon, J., 2017. Rocking Chair Desalination Battery Based on Prussian Blue Electrodes. ACS Omega 2, 1653–1659. https://doi.org/10.1021/acsomega.6b00526

Lim, J.-A., Park, N.-S., Park, J.-S., Choi, J.-H., Jung-Ae, L., Nam-Soo, P., Jin-Soo, P., Jae-Hwan, C., 2009. Fabrication and characterization of a porous carbon electrode for desalination of brackish water. Desalination 238, 37–42. https://doi.org/http://dx.doi.org/10.1016/j.desal.2008.01.033

Liu, S., Smith, K.C., 2018. Quantifying the Trade-offs between Energy Consumption and Salt Removal Rate in Membrane-free Cation Intercalation Desalination. Electrochim. Acta 271, 652–665. https://doi.org/10.1016/j.electacta.2018.03.065

Liu, Y., Gao, X., Wang, Z., Wang, K., Dou, X., Zhu, H., Yuan, X., Pan, L., 2021. Controlled synthesis of bismuth oxychloride-carbon nanofiber hybrid materials as highly efficient electrodes for rocking-chair capacitive deionization. Chem. Eng. J. 403, 126326. https://doi.org/10.1016/j.cej.2020.126326

Malifarge, S., Delobel, B., Delacourt, C., 2017. Determination of Tortuosity Using Impedance Spectra Analysis of Symmetric Cell. J. Electrochem. Soc. 164, 3329–3334. https://doi.org/10.1149/2.0331711jes

Maria, A., Mouas, M., Videcoq, A., Cerbelaud, M., Bienia, M., Bowen, P., Ferrando, R., 2015. How colloid – colloid interactions and hydrodynamic effects influence the percolation threshold : A simulation study in alumina suspensions. J. Colloid Interface Sci. 458, 241–246. https://doi.org/10.1016/j.jcis.2015.07.058

Mauter, M.S., Fiske, P.S., 2020. Desalination for a circular water economy. Energy Environ. Sci. 13, 3180–3184. https://doi.org/10.1039/d0ee01653e

Mekonnen, M.M., Hoekstra, A.Y., 2016. Four billion people facing severe water scarcity. Sci. Adv. 2, e1500323. https://doi.org/10.1126/sciadv.1500323

Metzger, M., Besli, M.M., Kuppan, S., Hellstrom, S., Kim, S., Sebti, E., Subban, C. V., Christensen, J., 2020. Techno-economic analysis of capacitive and intercalative water deionization. Energy Environ. Sci. 13, 1544–1560. https://doi.org/10.1039/d0ee00725k

Patel, S.K., Ritt, C.L., Deshmukh, A., Wang, Z., Qin, M., Epsztein, R., Elimelech, M., 2020. The relative insignificance of advanced materials in enhancing the energy efficiency of desalination technologies. Energy Environ. Sci. 13, 1694–1710. https://doi.org/10.1039/d0ee00341g

Porada, S., Shrivastava, A., Bukowska, P., Biesheuvel, P.M., Smith, K.C., 2017. Nickel Hexacyanoferrate Electrodes for Continuous Cation Intercalation Desalination of Brackish Water. Electrochim. Acta 255, 369–378. https://doi.org/10.1016/j.electacta.2017.09.137

Pothanamkandathil, V., Fortunato, J., Gorski, C.A., 2020. Electrochemical Desalination Using Intercalating Electrode Materials: A Comparison of Energy Demands. Environ. Sci. Technol. 54, 3653–3662. https://doi.org/10.1021/acs.est.9b07311

Reale, E.R., Shrivastava, A., Smith, K.C., 2019. Effect of conductive additives on the transport properties of porous flow-through electrodes with insulative particles and their optimization for Faradaic deionization. Water Res. 165, 114995. https://doi.org/10.1016/j.watres.2019.114995

Reale, E.R., Smith, K.C., 2018. Capacitive Performance and Tortuosity of Activated Carbon Electrodes with Macroscopic Pores. J. Electrochem. Soc. 165, A1685–A1693. https://doi.org/10.1149/2.0601809jes

Shrivastava, A., Smith, K.C., 2018. Electron Conduction in Nanoparticle Agglomerates Limits Apparent Na+ Diffusion in Prussian Blue Analogue Porous Electrodes. J. Electrochem. Soc. 165, A1777. https://doi.org/10.1149/2.0861809jes

Singh, B.P., Menchavez, R., Takai, C., Fuji, M., Takahashi, M., 2005. Stability of dispersions of colloidal alumina particles in aqueous suspensions. J. Colloid Interface Sci. 291, 181–186. https://doi.org/10.1016/j.jcis.2005.04.091

Singh, K., Qian, Z., Biesheuvel, P.M., Zuilhof, H., Porada, S., 2020. Nickel hexacyanoferrate electrodes for high mono/divalent ion-selectivity in capacitive deionization. Desalination 481, 114346. https://doi.org/10.1016/j.desal.2020.114346

Sis, H., Birinci, M., 2017. Effect of nonionic and ionic surfactants on zeta potential and dispersion properties of carbon black powders. Colloids Surfaces A Physicochem. Eng. Asp. https://doi.org/10.1016/j.colsurfa.2009.03.039

Smith, K.C., 2017. Theoretical evaluation of electrochemical cell architectures using cation intercalation electrodes for desalination. Electrochim. Acta 230, 333–341. https://doi.org/10.1016/j.electacta.2017.02.006

Smith, K.C., Dmello, R.D., 2016. Na-Ion Desalination (NID) Enabled by Na-Blocking Membranes and Symmetric Na-Intercalation: Porous-Electrode Modeling. J.

Electrochem. Soc. 163, A530–A539. https://doi.org/10.1149/2.0761603jes

Son, M., Pothanamkandath, V., Yang, W., Gorski, C.A., Logan, B.E., 2020. Improving the Thermodynamic Energy Efficiency of Battery Electrode Deionization Using Flow-Through Electrodes. Environ. Sci. Technol. https://doi.org/10.1021/acs.est.9b06843

Subramani, A., Jacangelo, J.G., 2014. Treatment technologies for reverse osmosis concentrate volume minimization: A review. Sep. Purif. Technol. 122, 472–489. https://doi.org/10.1016/j.seppur.2013.12.004

Suss, M.E., Porada, S., Sun, X., Biesheuvel, P.M., Yoon, J., Presser, V., 2015. Water desalination via capacitive deionization: what is it and what can we expect from it? Energy Environ. Sci. 8, 2296–2319. https://doi.org/10.1039/C5EE00519A

Tang, W., Liang, J., He, D., Gong, J., Tang, L., Liu, Z., 2019. Various cell architectures of capacitive deionization : Recent advances and future trends. Water Res. 150, 225–251. https://doi.org/10.1016/j.watres.2018.11.064

Thormann, E., 2012. On understanding of the Hofmeister effect: How addition of salt alters the stability of temperature responsive polymers in aqueous solutions. RSC Adv. 2, 8297–8305. https://doi.org/10.1039/c2ra20164j

van Bommel, A., Divigalpitiya, R., 2012. Effect of Calendering LiFePO4 Electrodes. J. Electrochem. Soc. 159, A1791–A1795. https://doi.org/10.1149/2.029211jes

Zhu, M., Park, J., Sastry, A.M., 2011. Particle Interaction and Aggregation in Cathode Material of Li-Ion Batteries: A Numerical Study. J. Electrochem. Soc. 158, A1155. https://doi.org/10.1149/1.3625286

Zhu, M., Park, J., Sastry, A.M., Lu, W., 2014. Numerical Study of Interaction and

Aggregation of Non-Spherical Particles in Forming Li-Ion Battery Cathodes. J. Electrochem. Soc. 161, A1247–A1252. https://doi.org/10.1149/2.0211409jes

Zolin, L., Chandesris, M., Porcher, W., Lestriez, B., 2019. An Innovative Process for Ultra-Thick Electrodes Elaboration: Toward Low-Cost and High-Energy Batteries. Energy Technol. 7, 1–11. https://doi.org/10.1002/ente.201900025